Supplementary of

Chlorine enhances nocturnal heterogeneous uptake of NO_2 in coastal atmosphere under sea-land breeze circulation

Ziyi Lin[1,2,3], Xiuwen Yong[1,2,4], Lingjun Li[1,2,3], Yuping Chen[1,2,3], Lingling Xu[1,2,3]*, Xiaoting Ji[1,2,3], Chen Yang[1,2,3], Keran Zhang[1,2,3], Feng Zhang,[1,2] Ziying Chen[1,2,3], Gaojie Chen[1,2,3], Xiaolong Fan[1,2], Mengren Li[1,2], Jinsheng Chen[1,2,3]*

Affiliations:

[1]State Key Laboratory of Advanced Environmental Technology, Institute of Urban Environment, Chinese Academy of Sciences, Xiamen 361021, China
[2]Fujian Key Laboratory of Atmospheric Ozone Pollution Prevention, Institute of Urban Environment, Chinese Academy of Sciences, Xiamen 361021, China
[3]University of Chinese Academy of Sciences, Beijing 100049, China
[4]Fujian Agriculture and Forestry University, Fuzhou, 350002, China

*Correspondence to: jschen@iue.ac.cn (Jinsheng Chen); Linglingxu@iue.ac.cn (Lingling Xu)

TABLE OF CONTENTS

Number of Texts: 3

Number of Tables: 4

Number of Figures: 12

List of the Supporting information:

Text S1. Detailed information of measurements

More details for HONO detector, chemical ionization time-of-flight mass spectrometer, and ACSM are provided below. During this field campaign, the concentration of HONO was measured by a water-based long-path absorption photometer (Zhichen Beijing, China) with the detection limit of 1.7 ppt at a response time of 5 s, which has been widely used in previous field observations (Xuan et al., 2024; Xuan et al., 2023). Ambient HONO was sampled into a double-channel spiral tube, absorbed by ultra-pure water, and then mixed with derivative solution (near 2 mmol/L sulfanilamide, 144 mmol/L HCl and 77 μmol/L N-(1-naphthyl) ethylenediamine dihydrochloride) to form the azo dye derivative, which entered the liquid waveguide capillary cell (LWCC, WPI, USA) for detection using a fiber optic spectrometer (USB4000, OceanOptics, USA). The temperature of the sampling unit was controlled at 25 ℃ by a water bath. The liquid flow rate was 0.4mL/min and the sampling gas flow rate was 1L/min.

The chemical ionization atmospheric-pressure interface long time-of-flight mass spectrometer (CI-APi-LTOF, Aerodyne Research, Inc) was operated according to the procedures described in our previous study (Yang et al., 2023). A stainless-steel tube with length of 1.0 m and a diameter of 3/4 inch was used for sampling. The sample flow was kept constant throughout the campaign at approximately 8 L/min. The sheath flow is produced by combining a 20 L/min pure airflow with a 3 mL/min ultrahigh purity nitrogen flow containing nitric acid. This mixture is then passed through a Photoionization X-Ray (Model L9491, Hamamatsu, Japan) to create charged nitrate reagent ions. Gas-phase molecules, such as Sulfuric acid (H_2SO_4) and gaseous hydrogen chloride (HCl) are ionized to create deprotonated ions cluster with nitrate in the chamber where the ion-molecule reactions occur. Through a critical orifice with a diameter of 350μm, 0.8 L/min of mixed flow was pushed into the API-LTOF, where the analyzer can identify charged ions. The tofTools package (version 6.11), a collection of MATLAB-based software applications, was used to process the mass spectra. The concentration of H_2SO_4 and HCl were determined by equation 1, and equation 2.

$$[H_2SO_4]=\frac{HSO_4^-+H_2SO_4NO_3^-+H_2SO_4HSO_4^-}{NO_3^-+HNO_3NO_3^-+HNO_3HNO_3NO_3^-}\times C_1 \quad (1)$$

$$[HCl]=\frac{HClNO_3^-+Cl^-}{NO_2^-+O_2^-}\times C_2 \quad (2)$$

where C_1 and C_2 are the calibration coefficients (in units of molecules cm^{-3}), and the HSO_4^-, $H_2SO_4NO_3^-$, $H_2SO_4HSO_4^-$, NO_3^-, $HNO_3NO_3^-$, $HNO_3HNO_3NO_3^-$, $HClNO_3^-$, Cl^-, NO_2^- and O_2^- represent the signals of corresponding ions in units of counts per second (cps). As our previous studies (Yang et al., 2023; Fan et al., 2021), the calibration of H_2SO_4 was based on a calibration box that could produce a known concentration of H_2SO_4, and the calibration of HCl was used a semi-quantitative estimation. For H_2SO_4, A calibration factor (C_1) of 4.4×10^9 cm^{-3} was determined using a calibration device identical to that of Guo et al. (2021) (Guo et al., 2021), following the methodology established by Kürten et al. (2012) (Kürten et al., 2012). For HCl, the concentrations of HCl measured by the MARGA (Applikon Analytical B.V, Netherlands) were used to indirectly calibrate the HCl measured by the CI-APi-LTOF, and the obtained calibration factor (C_2) was 1.5×10^9 cm^{-3}.

The ACSM was used to measure chemical composition of non-refractory submicron aerosols including organic aerosol, nitrate, sulfate, ammonium, and chloride. Details of ACSM instrument operation can be found in our previous work (Chen et al., 2022). Briefly, aerosols were sampled at the main inlet at a flow rate of 3L/min and dried using a Nafion dryer system (Perma Pure, New

Jersery, USA) to keep the RH below 40%. A subsample flow of 0.085 L/min passed through a critical orifice and entered an aerodynamic lens that focused the particles into a narrow beam. Particles were then flash-vaporized at 600 ℃ in high vacuum conditions and ionized by hard-electron impact (70 eV), and the resulting fragments were analyzed by a quadrupole mass spectrometer. The time resolution of ACSM was about 15 min with a scan from m/z 10-150 atomic mass unit. The ionization efficiency and relative ion efficacy calibrations were performed using size-selected ammonium nitrate (NH_4NO_3) and ammonium sulfate ($(NH_4)_2SO_4$) particles (300 nm) by a differential particle counter.

Detailed descriptions of additional auxiliary measurements are described as following. Trace gases (O_3, NO*x*, SO_2 and CO) were monitored by Thermo models 49*i*, 17*i*, 43*i* and 48*i*. $PM_{2.5}$ was measured by a Thermo 1405DF (Thermo Fisher Scientific, Waltham, MA, USA). Meteorological parameters (T, RH, P, UV, and wind speed) were recorded with an integrated sensor (150WX, Airmar, USA). The photolysis frequencies (JO^1D, JNO_2, JHONO, JNO_3, JHCHO and JH_2O_2) were determined using a photolysis spectrometer (FPS-100, Focused Photonics Inc., Hangzhou, China). Additionally, approximately 116 VOCs were analyzed by a gas chromatography-mass spectrometer (GC-FID/MS, Agilent 7890B/6977, China). The detailed monitoring procedure, detection uncertainty and detection limit were shown in our previous studies (Liu et al., 2022a; Liu et al., 2020a; Liu et al., 2020b; Hu et al., 2020).

Text S2. Hyperparameter configurations and evaluations of Random Forest model

Similar to our previous work (Lin et al., 2025), the hyperparameters were tuned and selected using the grid search method. For the key hyperparameters of the RF model in this study, the number of trees was 150, the max depth was 10 and the min sample split was set as 3. The established model was evaluated by three statistical indicators including R^2 value, Mean Absolute Error (MAE) and Root Mean Square Error (RMSE). The R^2 is used to judge the goodness of fit between the predicted and observed results. The MAE provides a measure of predicted and observed results. And the RMSE characterizes the predictive accuracy of the model. The equations to calculate R^2, MAE and RMSE are equation 3, equation 4 and equation 5, respectively.

$$R^2=1-\frac{\sum_{i=1}^{N}(y_i - y'_i)^2}{\sum_{i=1}^{N}(y_i - \overline{y})^2} \quad (3)$$

$$MAE=\sqrt{\frac{\sum_{i=1}^{N}(y_i - y'_i)^2}{N}} \quad (4)$$

$$RMSE=\frac{1}{N}\sum_{i=1}^{N}|y_i - y'_i|^2 \quad (5)$$

where y_i, y'_i, $\overline{y}$, and N refer to the actual value of the *i*-th sample, the simulated value of the *i*-th sample, the mean of the actual values of all samples, and N is the number of samples, respectively.

Text S3. The multiphase chemical box model

As our previous work (Lin et al., 2026), the multiphase box model was constructed by adding gas-aqueous equilibrium in aerosols, unifying units between gas-phase and aqueous-phase chemistry, and incorporating detailed heterogeneous and aqueous-phase chemical mechanisms. Comprehensive chemical mechanisms of HONO and NO_3^- (**Table. S1** and Table. S2) were

incorporated into the F0AM model to simulate the variations of HONO and NO_3^-. The kNO_2 used in the HONO and NO_3^- budgets was calculated as described in Methods. In terms of the scenario simulations, the mean diurnal pattern of trace gas concentrations (O_3, NO, NO_2, CO, SO_2, HCl, H_2SO_4, and VOCs), meteorological parameters (T, RH, P, BLH, and photolysis frequencies), as well as the results from the ISORROPIA II model during SLB days and non-SLB days were used as input data to constrain box model. A 3-day spin-up was set prior to each simulation to stabilize the concentration of intermediate species. In addition to chemical processes, physical loss processes including dry deposition and dilution were also considered in the model. The dry deposition velocities for the constrained species were set according to Liu et al (Liu et al., 2022b). And the basic dilution rate was set to 8×10^{-5} s^{-1}, varying with boundary layer height.

Table S1. Summary of the HONO mechanism incorporated in the F0AM.

Pathways	Reaction rate	References
Vehicle emissions	k = 0.5%×[NO*x*] (molec/cm^3/s)	(Zhang et al., 2025)
OH + NO → HONO	$k = k_{OH+NO}$	MCM v3.3.1
pNO_3^- + hv → HONO	$k = 3.0\times10^{-5}\times\frac{JNO_2}{JNO_{2,\,max}}$ (/s)	(Ye et al., 2017)
HONO ⇌ NO_2^- (HONO (aq))	$k_1 = H_{HONO}$ (mol/L/atm); $k_2 = k_{t,HONO}$ (/s)	(Liu et al., 2024)
$NO_2 + H_2O \rightarrow HONO + HNO_3$	$k = k_{NO2}$ (/s)	calculated kNO_2
HONO + hv → NO + OH	$k = J_{HONO}$ (/s)	MCM v3.3.1
HONO + OH → $H_2O + NO_2$	$k = k_{HONO+OH}$ (/s)	MCM v3.3.1
HONO Dilution	$k = 8\times10^{-5}\times\frac{BLH}{BLH_{max}}$ (/s)	(Wolfe et al., 2016)
HONO deposition	$k = \frac{v_d}{BLH}$, vd = 4 (cm/s)	(Zhang et al., 2003)

The $J_{NO_{2,\,max}}$ refers to the maximum of the daily NO_2 photolysis rate. The BLH_{max} refers to the maximum of the daily BLH.

Table S2. Summary of the particulate nitrate mechanism incorporated in the F0AM.

Pathways	Reaction rate	References
$OH + NO_2 \rightarrow HNO_3 \xrightarrow{partition} pNO_3^-$	$k = k_{OH+NO2}\times$partition	MCM v3.3.1, ISORROPIA-II
$N_2O_5 + H_2O/Cl^- \rightarrow pNO_3^- + ClNO_2$	$k = 1/4\times\gamma N_2O_5\times S_{aerosol}\times c_{N2O5}$	(Evans and Jacob, 2005; Hallquist et al., 2003)
$NO_2 + H_2O \rightarrow HONO + HNO_3$	$k = k_{NO2}$ (/s)	calculated kNO_2
pNO_3^- + hv → HONO	$k = 3\times10^{-5}\times\frac{JNO_2}{JNO_{2,\,max}}$ (/s)	(Ye et al., 2017)
N_2O_5 deposition	$k = \frac{v_d}{BLH}$, vd = 2 (cm/s)	(Kim et al., 2014)
pNO_3^- deposition	$k = \frac{v_d}{BLH}$, vd = 0.1 (cm/s)	(Zhang et al., 2003)

Notably, the partition ratio is derived from the ISORROPIA-II model. The uptake coefficient (γ) is obtained from a parameterization method. Specifically, the γ is calculated by $\alpha \times 10^{\beta}$; α is $2.79 \times 10^{-4} + 1.3 \times 10^{-4} \times RH - 3.43 \times 10^{-6} \times RH^2 + 7.52 \times 10^{-8} \times RH^3$; and β is $4 \times 10^{-2} \times (T - 294)$ ($T > 282K$); $\beta = -0.48$ ($T < 282K$). The S_a and $c_{N_2O_5}$ are aerosol surface areas and mean molecular speed of N_2O_5, respectively.

Table S3. Descriptive statistic of the measured atmospheric species during nocturnal SLB and non-SLB periods. Notably, the observational data used was from 18:00 LT to 06:00 LT.

Species	SLB period	Non-SLB period
HONO (ppb)	0.836 ± 0.679	0.497 ± 0.387
NO (ppb)	5.10 ± 8.54	3.93 ± 6.02
NO_2 (ppb)	28.3 ± 12.3	23.2 ± 11.4
SO_2 (ppb)	4.71 ± 0.727	4.62 ± 0.651
O_3 (ppb)	25.4 ± 14.6	27.9 ± 15.8
OH (molec/cm^3)	$3.26 \times 10^5 \pm 3.84 \times 10^5$	$1.64 \times 10^5 \pm 1.48 \times 10^5$
HCl (ppt)	96.2 ± 50.0	67.5 ± 35.5
NO_3^- (μg/m^3)	3.61 ± 2.72	3.13 ± 2.35
Cl^- (μg/m^3)	0.154 ± 0.152	0.139 ± 0.150
NH_4^+ (μg/m^3)	1.45 ± 0.90	1.37 ± 0.857
SO_4^{2-} (μg/m^3)	2.87 ± 1.73	2.91 ± 1.52
T (K)	291 ± 3.14	289 ± 3.74
RH (%)	67.2 ± 10.7	62.2 ± 13.5
SA (μm^2/cm^3)	189 ± 71.3	146 ± 70.9

Table S4. The start and end times of the continuous increase of $HONO_{corr}/NO_2$. A total of 17 sustained increase events were identified during the observed 23 SLB days.

Events	Start time	End time	r	Slope (5min^{-1})
1	2023-11-19 22:05:00	2023-11-20 04:40:00	0.84	0.0016
2	2023-11-20 21:00:00	2023-11-21 01:45:00	0.79	0.0031
3	2023-11-21 18:20:00	2023-11-21 23:35:00	0.95	0.0029
4	2023-12-02 22:35:00	2023-12-03 03:35:00	0.77	0.0021
5	2023-12-07 19:05:00	2023-12-08 03:25:00	0.94	0.0050
6	2023-12-08 20:20:00	2023-12-09 04:00:00	0.72	0.0027
7	2023-12-09 21:15:00	2023-12-10 02:20:00	0.83	0.0039
8	2023-12-11 21:00:00	2023-12-12 03:40:00	0.79	0.0086
9	2023-12-13 19:00:00	2023-12-14 00:55:00	0.89	0.0003
10	2023-12-14 18:00:00	2023-12-14 22:50:00	0.73	0.0049
11	2023-12-15 21:05:00	2023-12-16 01:55:00	0.84	0.0094
12	2023-12-24 23:00:00	2023-12-25 04:15:00	0.76	0.0053
13	2023-12-26 21:00:00	2023-12-27 04:20:00	0.85	0.0021
14	2023-12-27 22:50:00	2023-12-28 03:35:00	0.89	0.007
15	2023-12-28 21:00:00	2023-12-29 04:55:00	0.85	0.0034
16	2024-01-05 18:00:00	2024-01-06 04:05:00	0.91	0.0031
17	2024-01-06 19:25:00	2024-01-06 21:40:00	0.94	0.0056

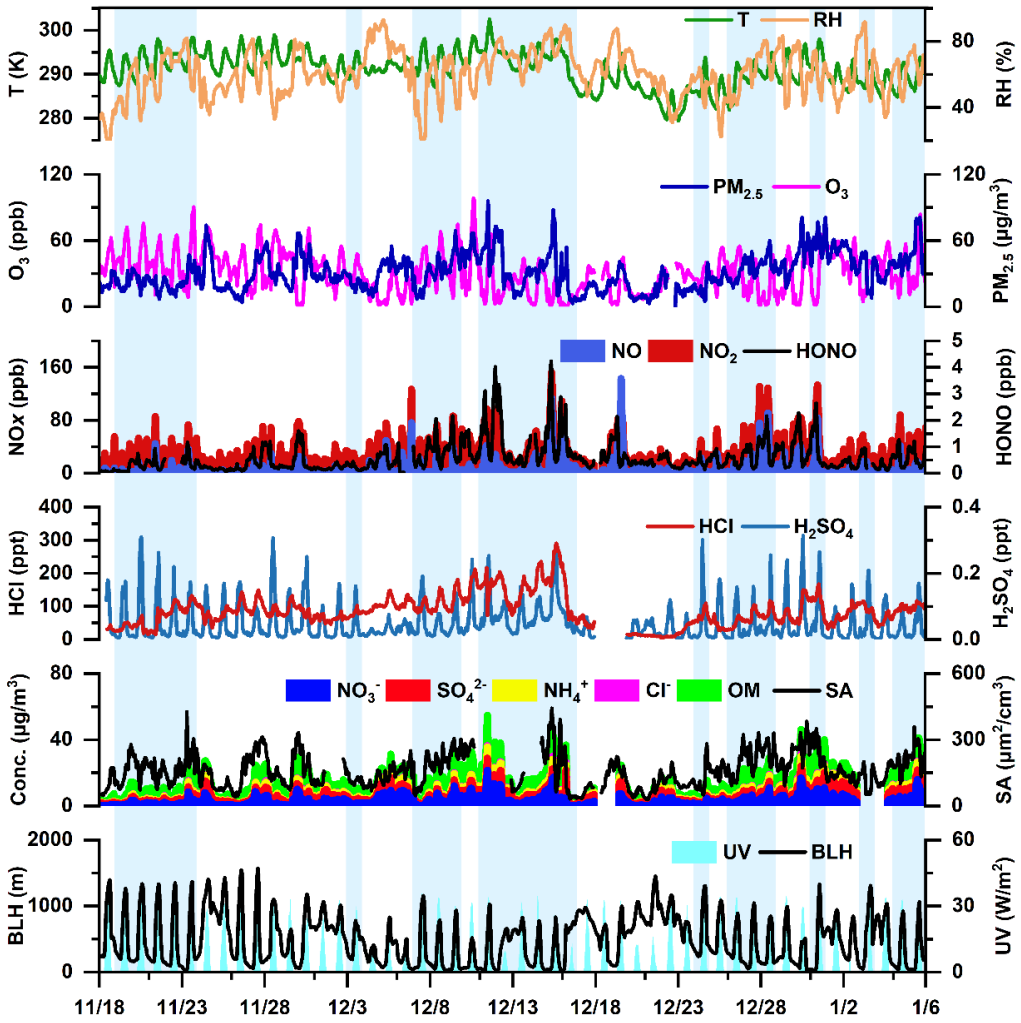

Figure S1. Time series of field observational parameters from November 18, 2023 to January 6, 2024. (a) ambient temperature (T) and relative humidity (RH), (b) O_3 and $PM_{2.5}$, (c) NO*x* and HONO, (d) HCl and H_2SO_4, (e) Main chemical components in $PM_{2.5}$ and aerosol surface area concentrations (SA), and (f) boundary layer height (BLH) and ultraviolet radiation (UV). The light blue shaded areas indicate sea-land breeze days.

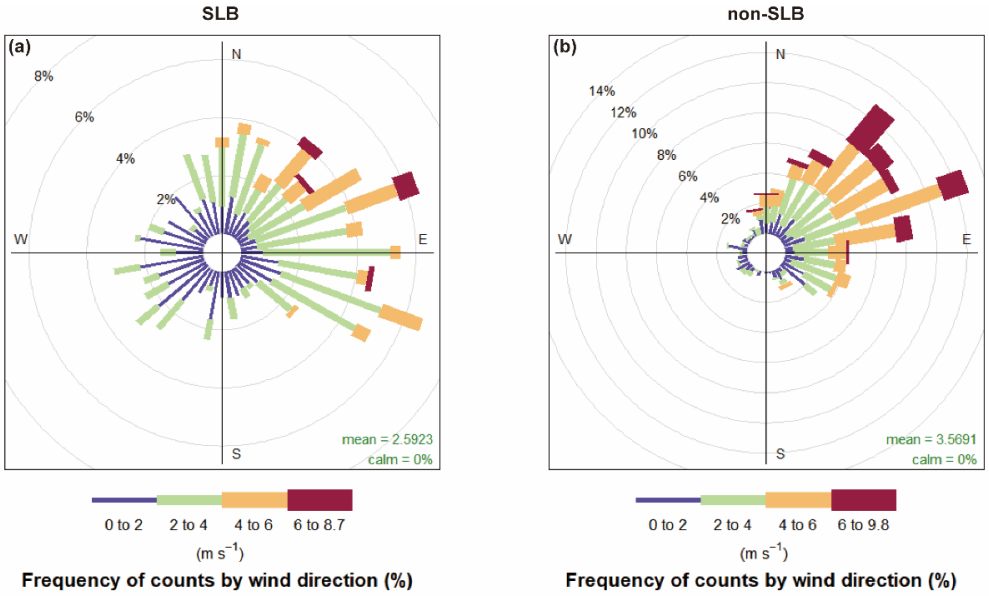

Figure S2. Comparison of the wind speed and wind direction between (a) SLB and (b) non-SLB days.

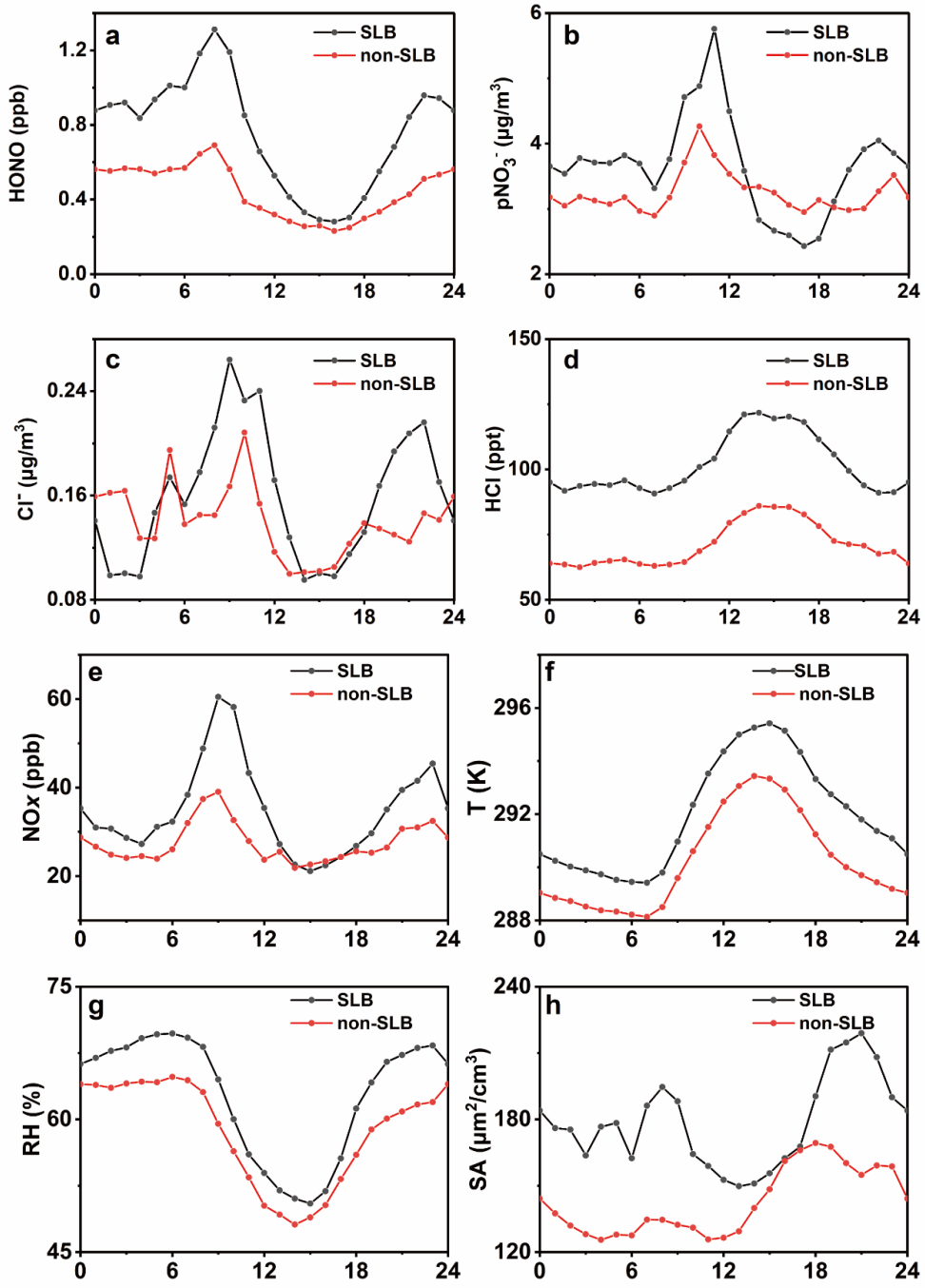

Figure S3. Diurnal patterns of major observed parameters on SLB and non-SLB days. The parameters included (a) HONO, (b) particulate nitrate, (c) Cl^-, (d) HCl, (e) NO*x*, (f) T, (g) RH, (h) SA.

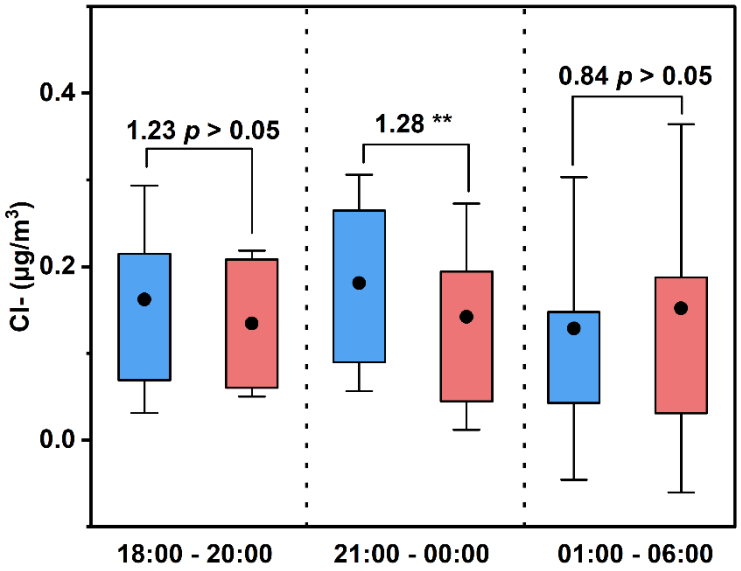

Figure S4. Box plots of the observed Cl^- at different nighttime periods including sea breeze period (18:00-20:00 LT), mixed sea-land breeze period (21:00-00:00 LT), and land breeze period (01:00-06:00 LT) during SLB (blue) and non-SLB days (red). Boxes show the 25th–75th percentiles with whiskers representing ± 1 standard deviation. The black dots inside the box represent the mean value.

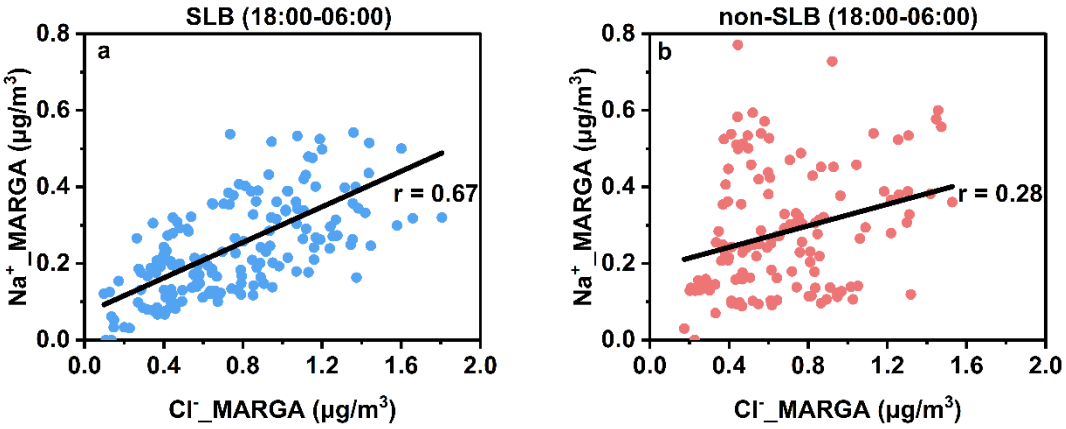

Figure S5. Correlation between sodium and chloride ions in $PM_{2.5}$ during nighttime on (a) SLB and (b) non-SLB days.

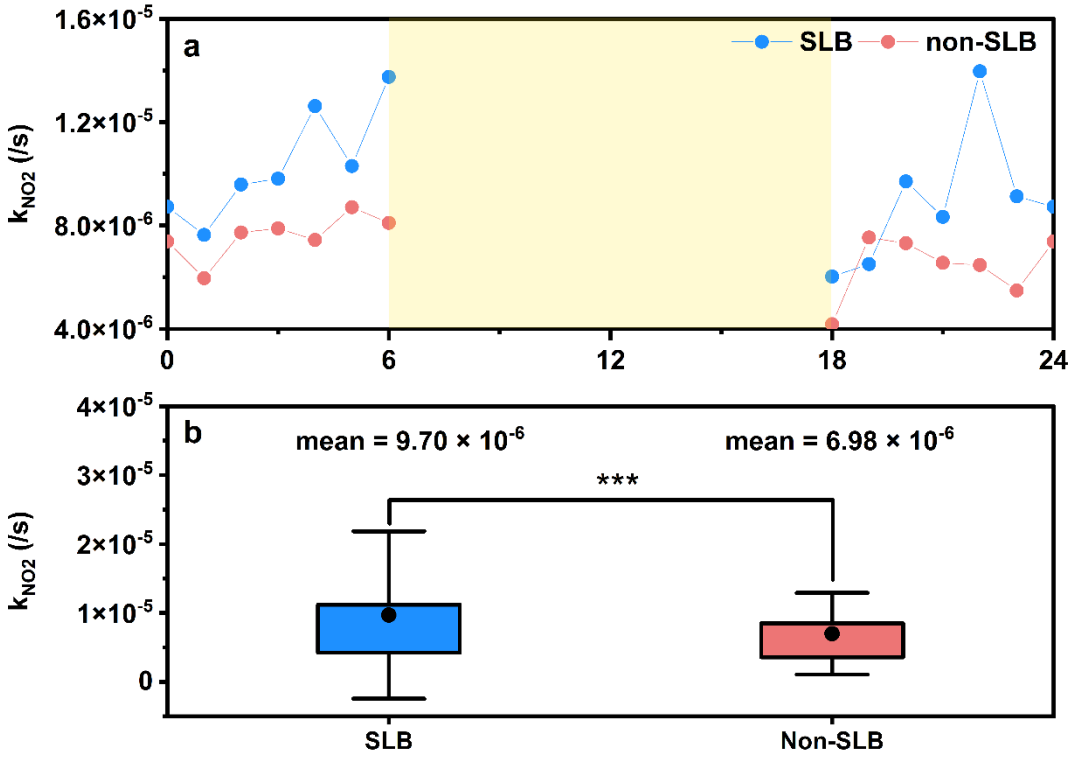

Figure S6. The kNO_2 derived from the variation of $HONO_{corr}/NO_2$ on SLB and non-SLB days. (a) nocturnal variations of kNO_2, and (b) the difference of kNO_2 between SLB days and non-SLB days. The box shows the 25th–75th percentiles; the whisker denotes ±1 standard deviation; the black solid circle inside the box represents the mean value. Differences between SLB and non-SLB days were tested using a two-sample t-test.

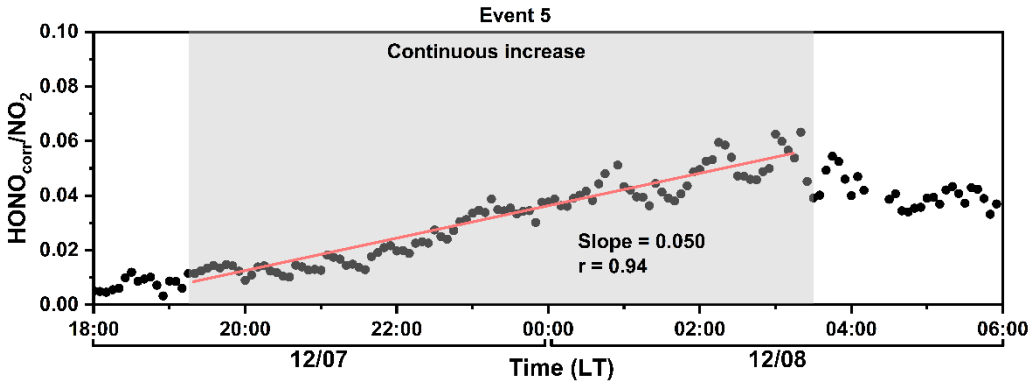

Figure S7. Temporal evolution of $HONO_{corr}/NO_2$ and its linear fit during SLB days, using Event 5 as an example.

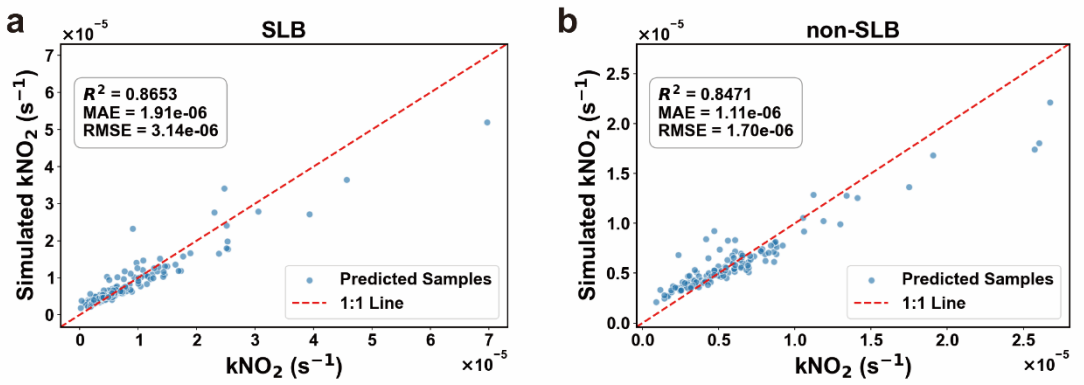

Figure S8. Performance of the random forest model. Model performance on (a) SLB days and (b) non-SLB days.

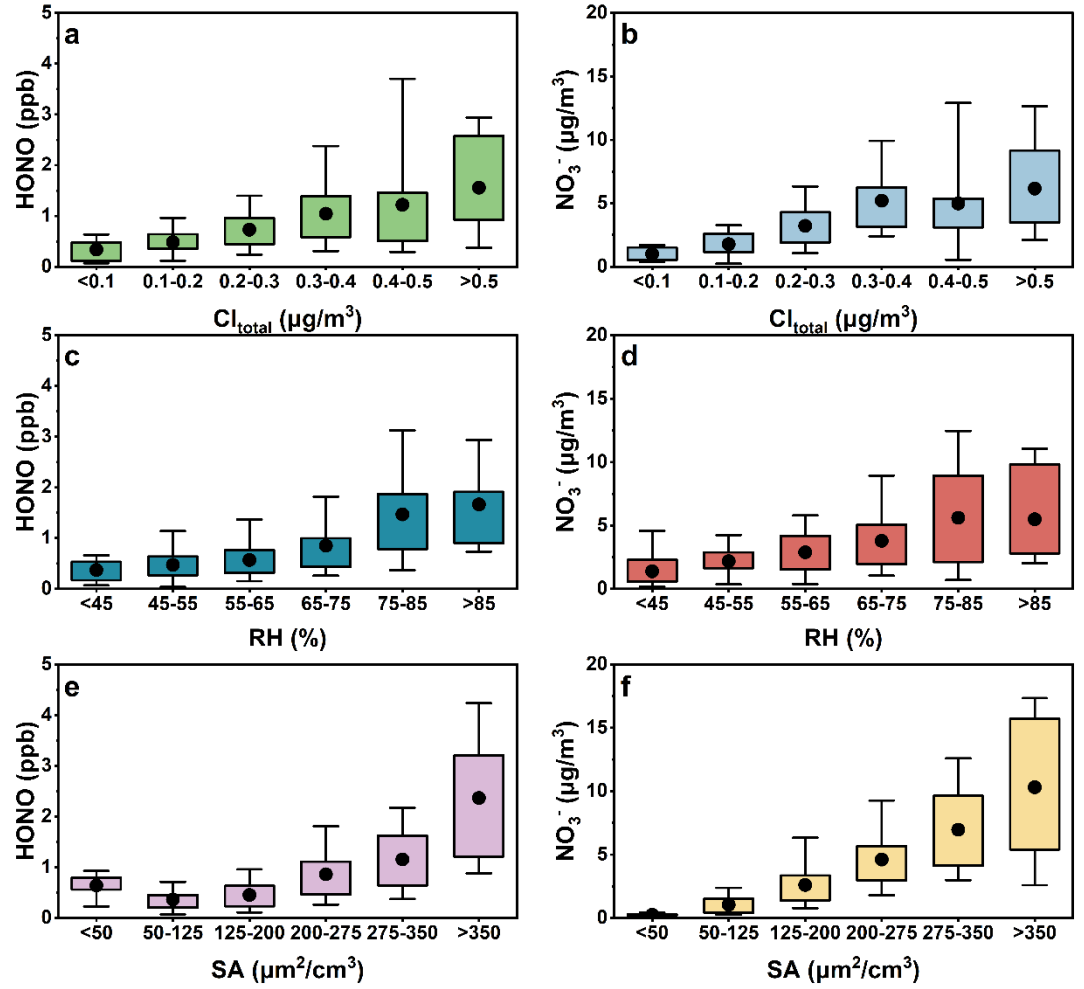

Figure S9. Dependence of the products of NO_2 uptake on influencing factors during SLB days. Variations of HONO and NO_3^- under different levels of (a) Cl_{total} (gaseous HCl + particulate Cl^-), (b) RH, and (c) surface area concentration (SA), using observational data from 18:00 to 06:00 LT. The box shows the 25th–75th percentiles; the whisker denotes 5th–95th percentiles; the black solid circle inside the box represents the mean value.

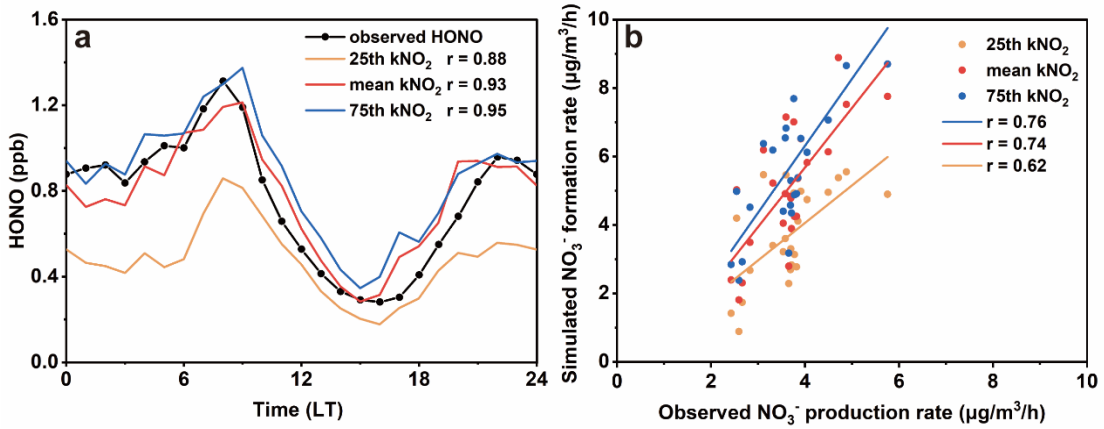

Figure S10. Multiphase chemical box model performance across different quantiles of kNO_2 reaction rates during SLB days. Simulated (a) HONO concentration and (b) NO_3^- production rates.

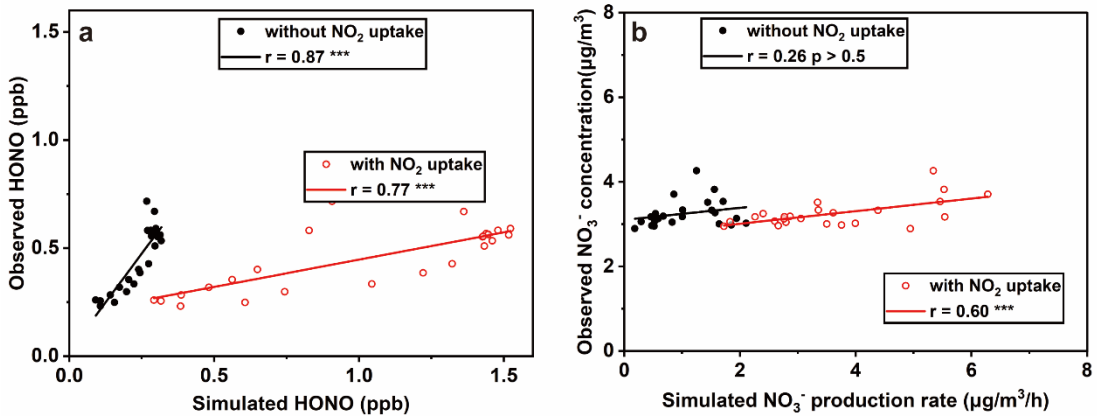

Figure S11. Multiphase chemical box model performance on non-SLB days with and without the heterogeneous NO_2 uptake mechanism. (a) simulated HONO and observed HONO concentrations, (b) simulated NO_3^- production rate and observed NO_3^- concentration.

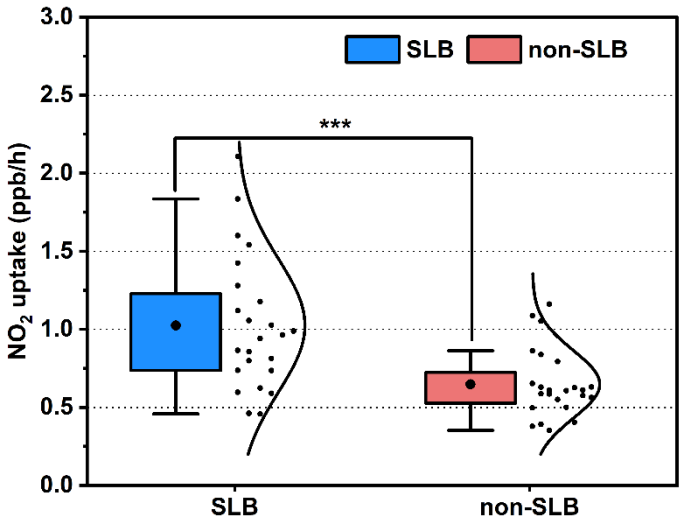

Figure S12. Model-derived reaction rates of NO_2 uptake on SLB and non-SLB days. The box shows the 25th–75th percentiles; the whisker denotes ±1 standard deviation; the black solid circle inside

the box represents the mean value. Differences between SLB and non-SLB days were tested using a two-sample t-test.

References:

Chen, Y., Yang, C., Xu, L., Chen, J., Zhang, Y., Shi, J., Fan, X., Zheng, R., Hong, Y., and Li, M.: Chemical composition of NR-PM_1 in a coastal city of Southeast China: Temporal variations and formation pathways, Atmospheric Environment. 285, 119243, https://doi.org10.1016/j.atmosenv.2022.119243, 2022.

Evans, M. J. and Jacob, D. J.: Impact of new laboratory studies of N_2O_5 hydrolysis on global model budgets of tropospheric nitrogen oxides, ozone, and OH, Geophysical Research Letters. 32, https://doi.org10.1029/2005GL022469, 2005.

Fan, X., Cai, J., Yan, C., Zhao, J., Guo, Y., Li, C., Dällenbach, K. R., Zheng, F., Lin, Z., Chu, B., Wang, Y., Dada, L., Zha, Q., Du, W., Kontkanen, J., Kurtén, T., Iyer, S., Kujansuu, J. T., Petäjä, T., Worsnop, D. R., Kerminen, V. M., Liu, Y., Bianchi, F., Tham, Y. J., Yao, L., and Kulmala, M.: Atmospheric gaseous hydrochloric and hydrobromic acid in urban Beijing, China: detection, source identification and potential atmospheric impacts, Atmos. Chem. Phys., 21, 11437-11452, https://doi.org/10.5194/acp-21-11437-2021, 2021.

Guo, Y., Yan, C., Li, C., Ma, W., Feng, Z., Zhou, Y., Lin, Z., Dada, L., Stolzenburg, D., Yin, R., Kontkanen, J., Daellenbach, K. R., Kangasluoma, J., Yao, L., Chu, B., Wang, Y., Cai, R., Bianchi, F., Liu, Y., and Kulmala, M.: Formation of nighttime sulfuric acid from the ozonolysis of alkenes in Beijing, Atmos. Chem. Phys., 21, 5499-5511, https://doi.org/10.5194/acp-21-5499-2021, 2021.

Hallquist, M., Stewart, D. J., Stephenson, S. K., and Anthony Cox, R.: Hydrolysis of N_2O_5 on sub-micron sulfate aerosols, Physical Chemistry Chemical Physics. 5, 3453-3463, https://doi.org/10.1039/B301827J, 2003.

Hu, B., Liu, T., Hong, Y., Xu, L., Li, M., Wu, X., Wang, H., Chen, J., and Chen, J.: Characteristics of peroxyacetyl nitrate (PAN) in a coastal city of southeastern China: Photochemical mechanism and pollution process, Science of The Total Environment. 719, 137493, https://doi.org/10.1016/j.scitotenv.2020.137493, 2020.

Kim, M. J., Farmer, D. K., and Bertram, T. H.: A controlling role for the air−sea interface in the chemical processing of reactive nitrogen in the coastal marine boundary layer, Proceedings of the National Academy of Sciences. 111, 3943-3948, https://doi.org/doi:10.1073/pnas.1318694111, 2014.

Kürten, A., Rondo, L., Ehrhart, S., and Curtius, J.: Calibration of a Chemical Ionization Mass Spectrometer for the Measurement of Gaseous Sulfuric Acid, The Journal of Physical Chemistry A. 116, 6375-6386, https://doi.org/10.1021/jp212123n, 2012.

Lin, Z., Ji, X., Xu, L., Chen, G., Yang, C., Zhang, K., Zhang, F., Li, L., Chen, Y., and Chen, J.: Enhanced NO_2-driven multiphase formation of particulate nitrate and sulfate under high-humidity conditions, npj Climate and Atmospheric Science. 9, 76, https://doi.org/10.1038/s41612-026-01352-5, 2026.

Lin, Z., Ying, C., Xu, L., Ji, X., Zhang, K., Zhang, F., Chen, G., Li, L., Yang, C., Chen, Y., Chen, Z., and Chen, J.: Measurement report: High contribution of N2O5 uptake to particulate nitrate formation in NO_2-limited urban areas, Atmos. Chem. Phys., 25, 17747-17759, https://doi.org/10.5194/acp-25-17747-2025, 2025.

Liu, L., Liu, X., Zhang, R., Gen, M., Chan, C. K., Song, S., and Wang, X.: Global Impact of Particulate Nitrate Photolysis on Fine Sulfate Aerosol, Environmental Science & Technology Letters. 11, 961-967, https://doi.org/10.1021/acs.estlett.4c00416, 2024.

Liu, T., Hu, B., Xu, X., Hong, Y., Zhang, Y., Wu, X., Xu, L., Li, M., Chen, Y., Chen, X., and Chen, J.: Characteristics of $PM_{2.5}$-bound secondary organic aerosol tracers in a coastal city in Southeastern China: Seasonal patterns and pollution identification, Atmospheric Environment. 237, 117710, https://doi.org/10.1016/j.atmosenv.2020.117710, 2020a.

Liu, T., Hu, B., Yang, Y., Li, M., Hong, Y., Xu, X., Xu, L., Chen, N., Chen, Y., Xiao, H., and Chen, J.: Characteristics and source apportionment of PM2.5 on an island in Southeast China: Impact of sea-salt and monsoon, Atmospheric Research. 235, 104786, https://doi.org /10.1016/j.atmosres.2019.104786, 2020b.

Liu, T., Chen, G., Chen, J., Xu, L., Li, M., Hong, Y., Chen, Y., Ji, X., Yang, C., Chen, Y., Huang, W., Huang, Q., and Wang, H.: Seasonal characteristics of atmospheric peroxyacetyl nitrate (PAN) in a coastal city of Southeast China: Explanatory factors and photochemical effects, Atmos. Chem. Phys., 22, 4339-4353, https://doi.org/10.5194/acp-22-4339-2022, 2022a.

Liu, T., Hong, Y., Li, M., Xu, L., Chen, J., Bian, Y., Yang, C., Dan, Y., Zhang, Y., Xue, L., Zhao, M., Huang, Z., and Wang, H.: Atmospheric oxidation capacity and ozone pollution mechanism in a coastal city of southeastern China: analysis of a typical photochemical episode by an observation-based model, Atmos. Chem. Phys., 22, 2173-2190, https://doi.org/10.5194/acp-22-2173-2022, 2022b.

Wolfe, G. M., Marvin, M. R., Roberts, S. J., Travis, K. R., and Liao, J.: The Framework for 0-D Atmospheric Modeling (F0AM) v3.1, Geosci. Model Dev., 9, 3309-3319, https://doi.org/10.5194/gmd-9-3309-2016, 2016.

Xuan, H., Zhao, Y., Ma, Q., Chen, T., Liu, J., Wang, Y., Liu, C., Wang, Y., Liu, Y., Mu, Y., and He, H.: Formation mechanisms and atmospheric implications of summertime nitrous acid (HONO) during clean, ozone pollution and double high-level $PM_{2.5}$ and O_3 pollution periods in Beijing, Science of The Total Environment. 857, 159538, https://doi.org /10.1016/j.scitotenv.2022.159538, 2023.

Xuan, H., Liu, J., Zhao, Y., Cao, Q., Chen, T., Wang, Y., Liu, Z., Sun, X., Li, H., Zhang, P., Chu, B., Ma, Q., and He, H.: Relative humidity driven nocturnal HONO formation mechanism in autumn haze events of Beijing, npj Climate and Atmospheric Science. 7, 193, https://doi.org/10.1038/s41612-024-00745-8, 2024.

Yang, C., Dong, H., Chen, Y., Wang, Y., Fan, X., Tham, Y. J., Chen, G., Xu, L., Lin, Z., Li, M., Hong, Y., and Chen, J.: Machine Learning Reveals the Parameters Affecting the Gaseous Sulfuric Acid Distribution in a Coastal City: Model Construction and Interpretation, Environmental Science & Technology Letters. 10, 1045-1051, https://doi.org/10.1021/acs.estlett.3c00170, 2023.

Ye, C., Zhang, N., Gao, H., and Zhou, X.: Photolysis of Particulate Nitrate as a Source of HONO and NOx, Environmental Science & Technology. 51, 6849-6856, https://doi.org/10.1021/acs.est.7b00387, 2017.

Zhang, L., Brook, J. R., and Vet, R.: A revised parameterization for gaseous dry deposition in air-quality models, Atmos. Chem. Phys., 3, 2067-2082, https://doi.org/10.5194/acp-3-2067-2003, 2003.

Zhang, Y., Liu, Y., Ma, W., Hua, C., Zheng, F., Lian, C., Wang, W., Xia, M., Zhao, Z., Li, J., Xie, J., Wang, Z., Wang, Y., Chen, X., Zhang, Y., Feng, Z., Yan, C., Chu, B., Du, W., Kerminen, V.-M., Bianchi, F., Petäjä, T., Worsnop, D., and Kulmala, M.: Changing aerosol chemistry is redefining HONO sources, Nature Communications. 16, 5238, https://doi.org/10.1038/s41467-025-60614-7, 2025.